# Localized thermonuclear bursts from accreting magnetic white dwarfs

https://doi.org/10.1038/s41586-022-04495-6

Received: 4 October 2021

Accepted: 1 February 2022

Published online: 20 April 2022



Check for updates

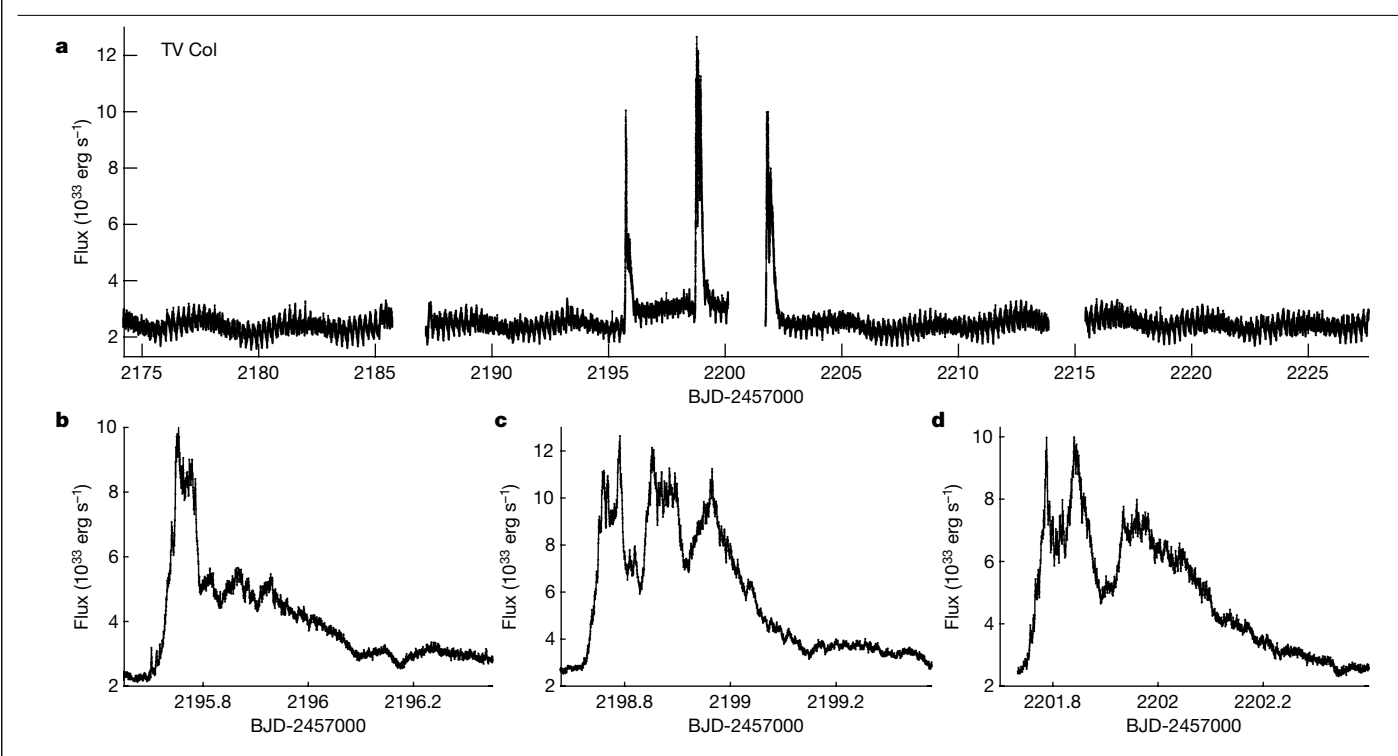
S. Scaringi<sup>1⊠</sup>, P. J. Groot<sup>2,3,4</sup>, C. Knigge<sup>5</sup>, A. J. Bird<sup>5</sup>, E. Breedt<sup>6</sup>, D. A. H. Buckley<sup>3,4,7</sup>, Y. Cavecchi<sup>8</sup>, N. D. Degenaar<sup>9</sup>, D. de Martino<sup>10</sup>, C. Done<sup>1</sup>, M. Fratta<sup>1</sup>, K. Iłkiewicz<sup>1</sup>, E. Koerding<sup>2</sup>, J.-P. Lasota<sup>11,12</sup>, C. Littlefield<sup>13,14</sup>, C. F. Manara<sup>15</sup>, M. O'Brien<sup>1</sup>, P. Szkody<sup>14</sup> & F. X. Timmes<sup>16,17</sup>

Nova explosions are caused by global thermonuclear runaways triggered in the surface layers of accreting white dwarfs<sup>1-3</sup>. It has been predicted<sup>4-6</sup> that localized thermonuclear bursts on white dwarfs can also take place, similar to type-IX-ray bursts observed in accreting neutron stars. Unexplained rapid bursts from the binary system TV Columbae, in which mass is accreted onto a moderately strong magnetized white dwarf from a low-mass companion, have been observed on several occasions in the past 40 years<sup>7-11</sup>. During these bursts, the optical/ultraviolet luminosity increases by a factor of more than three in less than an hour and fades in around ten hours. Fast outflows have been observed in ultraviolet spectral lines<sup>7</sup>, with velocities of more than 3,500 kilometres per second, comparable to the escape velocity from the white dwarf surface. Here we report on optical bursts observed in TV Columbae and in two additional accreting systems, El Ursae Majoris and ASASSN-19bh. The bursts have a total energy of approximately 10<sup>-6</sup> times than those of classical nova explosions (micronovae) and bear a strong resemblance to type-I X-ray bursts<sup>12–14</sup>. We exclude accretion or stellar magnetic reconnection events as their origin and suggest thermonuclear runaway events in magnetically confined accretion columns as a viable explanation.

TV Columbae (hereafter TV Col) has been extensively studied in the past at wavelengths ranging from optical to hard X-rays<sup>7-10</sup>. The orbital period of 5.5 h and the white dwarf spin period of approximately 1,900 s have been observed at both optical and X-ray wavelengths 15-17. During the bursts, high-ionization helium and nitrogen lines strengthen and a transient outflow with velocity of more than 3,500 km s<sup>-1</sup> is observed at peak luminosity, revealed by P-Cygni profiles in ultraviolet (UV) spectral lines<sup>7</sup>. El Ursae Majoris (hereafter El UMa) is also known to harbour a magnetic white dwarf accreting matter from a companion star, and both orbital and white dwarf spin periods have been identified at 6.4 h and approximately 746 s, respectively 18-20. ASASSN-19bh was recently discovered as a transient by ASAS-SN<sup>21,22</sup> on 25 January 2019, displaying a sudden increase in brightness of at least 2.1 mag. Extended Data Figure 1 shows the X-Shooter spectrum of ASASSN-19bh obtained on 1 October 2021, illustrating absorption lines from the donor star, and hydrogen Balmer and helium lines in emission. Although the emission lines are narrow when compared to some accreting white dwarfs (AWD), the X-Shooter spectrum shows ASASSN-19bh to be an AWD with a donor star compatible with a K-type star, similar to the long-period AWD<sup>23</sup> CXOGBS J175553.2-281633.

The Transiting Exoplanet Survey Satellite (TESS) observed TV Col during cycle 1 (15 November 2018 to 6 January 2019) at 120 s cadence and during cycle 3 (19 November 2019 to 13 January 2020) at 20 s cadence. EIUMawasobservedduringTESScvcle2(24December2019to20Ianuary 2020) at 120 s cadence and ASASSN-19bh during cycle 3 (5 July 2020 to 30 July 2020 and 29 April 2021 to 24 June 2021) at 120 s cadence. Figure 1 shows the observed TESS cycle 1 (sectors 32 and 33) lightcurves of TV Col with three consecutive bursts observed, each lasting approximately 12 h with a rise time of less than 30 min, and each burst separated by approximately 3 days. Figure 2 displays the observed TESS lightcurve of EI UMa during sector 20, showing two rapid and consecutive bursts each lasting approximately 7 h and separated by approximately 1 day. The brightness evolution and temporal properties resemble those observed in TV Col, displaying multiple peaks and throughs. Figure 2 also displays the TESS lightcurve of ASASSN-19bh observed during sector 38, showing a precursor followed by a single energetic burst with a rise time of approximately 1.5 h during which the luminosity increases by a factor of approximately 25 and decays over several days. In both Fig. 1 and Fig. 2 we have calibrated the observed TESS count rates into g-band equivalent luminosities using quasi-simultaneous

1centre for Extragalactic Astronomy, Department of Physics, Durham University, Durham, UK. 2Department of Astrophysics/IMAPP, Radboud University, Nijmegen, the Netherlands. 3South African Astronomical Observatory, Cape Town, South Africa. <sup>4</sup>Department of Astronomy, University of Cape Town, Rondebosch, South Africa. <sup>5</sup>School of Physics and Astronomy, University of Southampton, Southampton, UK, <sup>6</sup>Institute of Astronomy, University of Cambridge, Cambridge, UK, <sup>7</sup>Department of Physics, University of the Free State, Bloemfontein, South Africa, <sup>8</sup>Instituto de Astronomía, Universidad Nacional Autónoma de México, Ciudad de México, Mexico. Anton Pannekoek Institute for Astronomy, University of Amsterdam, Amsterdam, the Netherlands 10 INAF-Osservatorio Astronomico di Capodimonte, Naples, Italy. 11 Nicolaus Copernicus Astronomical Center, Polish Academy of Sciences, Warsaw, Poland. 12 Institut d'Astrophysique de Paris, CNRS et Sorbonne Universités, UMR 7095, Paris, France, 13 Department of Physics, University of Notre Dame, Notre Dame, IN, USA, 14 Department of Astronomy, University of Washington, Seattle, WA, USA. 15 European Southern Observatory, Garching, Germany. 16 School of Earth and Space Exploration, Arizona State University, Tempe, AZ, USA. 17 Joint Institute for Nuclear Astrophysics Center for the Evolution of the Elements, Notre Dame, IN, USA. ⊠e-mail: simone.scaringi@durham.ac.uk



 $\label{eq:Fig.1} Fig. 1 | Optical brightness variations in TV Col. a, TESS lightcurve (20 s cadence) of TV Col. The lightcurve has been calibrated against quasi-simultaneous ground-based ASAS-SN g-band data (Methods). <math>\mathbf{b}-\mathbf{d}$ , The

16.8 h of data around the three detected rapid bursts, with individual bursts yielding integrated energies of  $0.9\times10^{38}$  erg (**b**),  $1.6\times10^{38}$  erg (**c**) and  $1.0\times10^{38}$  erg (**d**).

ground-based g-band ASAS-SN observations 16,17 and distances inferred from the Gaia<sup>24,25</sup> measured parallaxes (Methods). We use the calibrated lightcurves to infer peak burst luminosities and total energy released by each burst. Without taking into account a bolometric correction, we constrain the mean peak luminosity of the bursts to be  $1.0 \times 10^{34} \text{ erg s}^{-1}$ ,  $2.5 \times 10^{34} \text{ erg s}^{-1}$  and  $3.5 \times 10^{34} \text{ erg s}^{-1}$  for TV Col, EI UMa and ASASSN-19bh, respectively. Integrating the burst luminosities, and summing the energies in the consecutive bursts observed in TV Col and EI UMa, yields burst energies of  $3.5 \times 10^{38}$  erg,  $5.2 \times 10^{38}$  erg and  $1.2 \times 10^{39}$  erg for TV Col, EI UMa and ASASSN-19bh, respectively. The luminosity rise gradient during the burst onset for all observed bursts in all three systems is determined to be in the range of 27–52 mag day<sup>-1</sup>  $(1.6-5.0\times10^{30}\,\mathrm{erg\,s^{-2}})$ , whereas the rate of decay is observed in the range of 1–3 mag day $^{-1}$  (0.8–5.3 × 10<sup>29</sup> erg s $^{-2}$ ). The TESS observations not only reveal that the rapid bursts observed in TV Col can sometimes occur in clusters, but also that these bursts, as determined by their temporal and energetic properties, are not limited to just TV Col. Furthermore, the long-term ASAS-SN monitoring of these sources (Extended Data Fig. 2) establishes these bursts as a recurring phenomenon.

A few scenarios have been proposed to explain the rapid bursts in TV Col, and by analogy we can attempt to apply these to EI UMa and ASASSN-19bh. One prominent model is that the bursts are driven by thermal-viscous instabilities in the disk, similar to so-called dwarf-nova outbursts observed in a range of subtypes of AWDs<sup>26,27</sup>. However, the much shorter duration of the bursts, and their occurrence in closely spaced clusters, invalidates this scenario<sup>11, 27</sup>. Another possibility may be that luminosity variations are induced by magnetically gated flares as observed in some weakly magnetized AWDs<sup>28,29</sup>. For this to happen, the disk would need to reach a specific mass transfer rate, and the bursts would appear as quasi-periodic, making this scenario also unlikely in explaining the observed bursts. Enhanced mass transfer events driven by an instability in the donor stars has also been suggested to explain the rapid bursts9. In this scenario, a short-lived enhanced mass transfer event would allow the stream of material to overflow the outer accretion disk edge. Our observations of consecutive bursts in TV Col and in EI UMa make this scenario also unlikely, as it would require the donor star to drive several consecutive instabilities that maintain their coherence while travelling through the outer accretion disk. Finally, low-mass stars similar to the donors in TV Col, EI UMa and ASASSN-19bh are known to sporadically release energy through stellar flares by magnetic reconnection events with bulk luminosities emitted in the TESS passband <sup>30–32</sup>. However, even the most energetic stellar flares observed to date release approximately four orders of magnitude less energy than TV Col and EI UMa, and approximately five orders of magnitude less than ASASSN-19bh <sup>33,34</sup>. We thus also exclude stellar flares as a candidate explanation for the observed rapid bursts.

The burst luminosity rise gradient for all observed bursts in all three systems is much faster than those observed in dwarf-nova outbursts and comparable to those observed in thermonuclear runaway (TNR) events such as classical nova explosions<sup>35,36</sup>. TESS also reveals how the time evolution of the individual bursts resembles TNR events occurring on the surface of accreting neutron stars, observed at X-ray wavelengths: type-IX-ray bursts<sup>12-14</sup>. The multi-peaked time evolution and the rapid succession of bursts observed in both TV Col and EI UMa mimic those observed in the X-ray binary neutron star 4U1636-536 (refs. <sup>37-39</sup>), slowed down by about three orders of magnitude. ASASSN-19bh also displays a resemblance to those more energetic single peaked type-IX-ray bursts<sup>12</sup>, and shares a similar precursor to the type-IX-ray burst observed in the neutron star X-ray binary SAX J1808.4-3658 (ref. 40; see also Extended Data Fig. 3). On close inspection, the first burst observed in TV Col by TESS (Fig. 1b) also reveals the presence of several precursors during the burst onset. Furthermore, the fast rise and slow decay observed in the TESS lightcurves is also analogous to what is observed in type-I X-ray bursts. All bursts observed by TESS have comparable burst energies to those observed in type-I bursts of  $10^{38}$ – $10^{39}$  erg. These observables form the basis for exploring the possibility that the rapid bursts observed may have a thermonuclear origin.

Given the short duration and the energies released by the bursts compared to nova explosions, the TNR must be restricted to burning a limited amount of material and confined to a fraction of the white

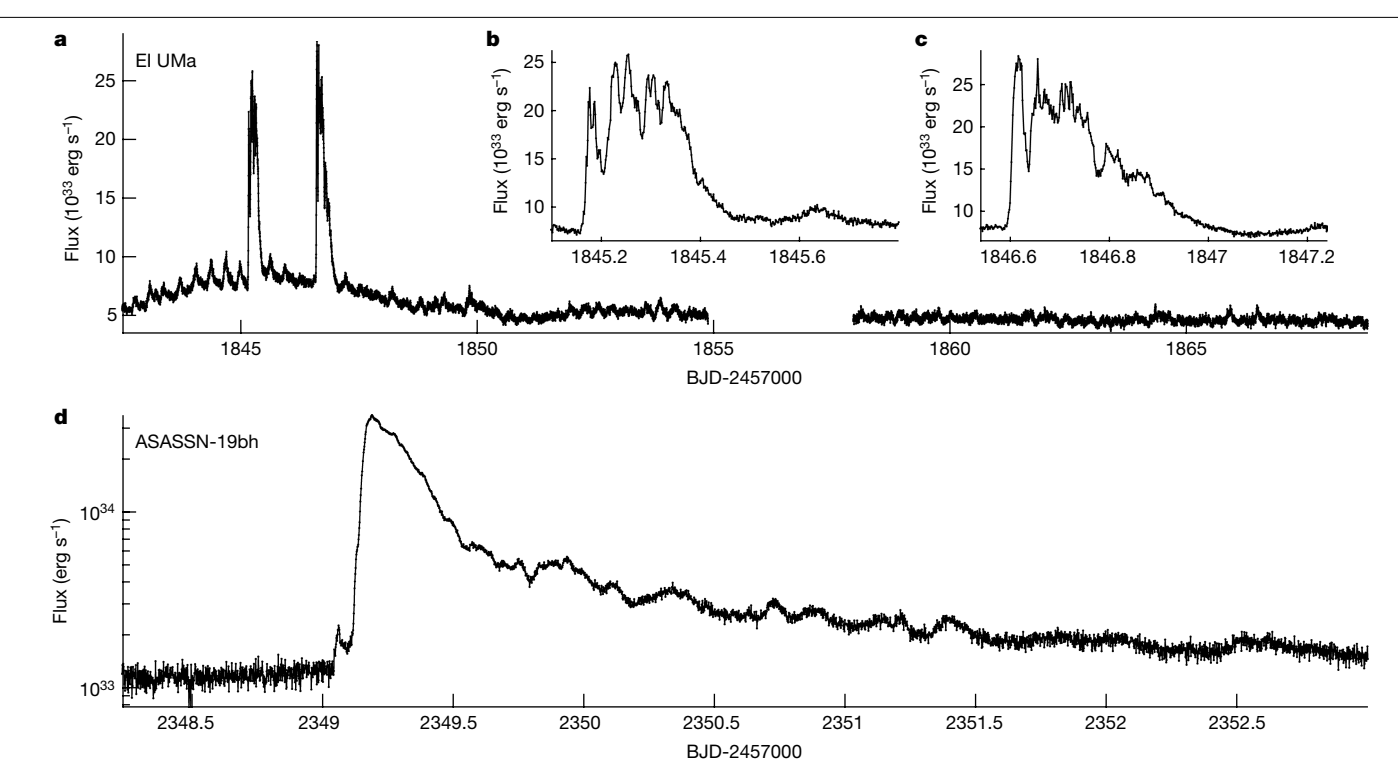


Fig. 2 | Optical brightness variations in El UMa and ASASSN-19bh. a. TESS lightcurve (2 min cadence) of EI UMa. b, c, The 16.8 h of data around the two detected rapid bursts, with individual bursts yielding integrated energies of  $2.4 \times 10^{38}$  erg (**b**) and  $2.8 \times 10^{38}$  erg (**c**). **d**, TESS lightcurve (2 min cadence) of

ASASSN-19bh showing the observed single energetic burst of  $1.2 \times 10^{39}$  erg. All lightcurves have been calibrated against quasi-simultaneous ground-based ASAS-SN g-band data (Methods).

dwarf surface<sup>4-6</sup>. In analogy with classical nova outbursts, to ignite hydrogen fuel on a carbon-oxygen white dwarf, the accreted material must reach a critical pressure at the base of the accreted layer of the order of  $P_{\rm crit} \approx 10^{18} - 10^{19}$  dyn cm<sup>-2</sup>, where the exact value will depend on the white dwarf mass (and thus also the radius 41), the temperature and the specific mass accretion rate per unit surface area<sup>3</sup>. In non-magnetic systems, this high pressure is generally achieved in AWDs when the spherical shell of accreted material reaches  $10^{-4}M_{\odot} - 10^{-6}M_{\odot}$ . The amount of accreted mass required to reach  $P_{crit}$  can be substantially reduced if accretion onto the white dwarf is confined to a much smaller fractional surface area<sup>4-6</sup>. If we take the mass-to-energy conversion for hydrogen-to-helium fusion in the carbon-nitrogen-oxygen cycle of approximately  $10^{16}$  erg  $g^{-1}$  we can infer a lower limit on the mass burned during the bursts in TV Col, EI UMa and ASASSN-19bh of approximately  $1.8 \times 10^{-11} M_{\odot}$ ,  $2.6 \times 10^{-11} M_{\odot}$  and  $5.8 \times 10^{-11} M_{\odot}$ , respectively, which are a factor of approximately  $10^{-6}$  lower than in classical novae.

Once triggered, a localized TNR will increase in temperature while burning through most of the freshly accreted layer. This process is also known to drive outflows (for example, classical novae<sup>1-3</sup>) with velocities comparable to, or higher than, the escape velocity of the AWD, after which the localized area is expected to drop back to the quiescent temperature. The sudden appearance of high ionization He II lines during the rise of two bursts observed in TV Col<sup>7,9</sup> is consistent with the presence of a hot ionizing source. The same lines weaken during the burst decay<sup>9</sup> and are entirely absent during quiescence<sup>7</sup>, indicating that the ionizing source fades and disappears. Furthermore, the bursts are observed to become bluer during the rise, which in turn suggests that the system must cool as it decays. Finally, high outflow velocities are observed only at the peak of the bursts<sup>7</sup>. All these observables are consistent with the interpretation that the bursts are in fact TNR events.

The cooling of an expanding photosphere following a TNR event has been observed in type-IX-ray bursts from accreting neutron stars14,37, providing a further analogy to what is observed in TV Col. Furthermore,

by analogy to type-I X-ray bursts, where very short waiting times are sometimes observed for the bursts<sup>14,42,43</sup>, the temporal evolution and short waiting times between the bursts in TV Col and EI UMa may be related to the energy from the TNR being released in steps. In the phenomenology of type-IX-ray bursts, the multi-peak behaviour and short recurrence times are explained as the result of partial burning at the base of the accreted column. This is thought to be driven by opacity changes due to temperature that drive convection in the column. In turn, this partially burns the column mass and then re-ignites it<sup>44</sup>. On the other hand, the precursor followed by the bright burst observed in ASASSN-19bh may indicate that the ignition at the base of the accretion column acts as a trigger that drives a shock front propagating and igniting the entire accumulated column mass in one energetic event. This mechanism has also been suggested to explain the precursor observed in the type-1 X-ray burst<sup>40</sup> of SAX J1808.4-3658. In the case of ASASSN-19bh, the precursor may thus be related to a shock breakout, somewhat similar to what is observed in a type-II supernova<sup>45</sup>. Alternatively, it may also be that the longer burst duration observed in ASASSN-19bh is somewhat analogous to the intermediate duration and superoutbursts observed in accreting neutron stars<sup>46</sup>.

With a white dwarf surface magnetic field  $B > 10^6$  G, as expected for TV Col and EI UMa, the spinning magnetosphere is able to govern the accretion dynamics and funnel material onto a smaller surface area,  $A_{\rm col.}$  creating an accretion column at the white dwarf magnetic poles 47,48. If the ram pressure from the infalling stream of material is comparable to the critical pressure required to ignite a TNR,  $P_{\text{ram}} \approx P_{\text{crit}}$ , a TNR can be expected. For this to happen, however, the fractional area,  $f = \frac{A_{\text{col}}}{A_{\text{WD}}}$ , has to be extremely small, of the order of  $f < 10^{-10}$  (Methods) when in general the fractional surface area is expected, and observed  $^{47,48}$ , to be  $10^{-2} > f > 10^{-7}$ . It is plausible that transverse temperature gradients and inhomogeneities in the accreted layers thermalize on timescales that are much longer than the TNR timescale. This prediction<sup>4,6</sup> is also expected to drive a localized TNR rather than a spherically symmetric global eruption.

The identification and characterization of rapid bursts in three AWDs have shown that magnetically confined TNRs may occur in the surface layers of white dwarf atmospheres. Similar bursts to those reported here have also been reported in the literature for other magnetic AWDs (for example, V1223 Sagittarii' and DW Cancri<sup>49</sup>) and it may be that localized TNRs on AWDs are more common than previously thought. Further observations of similar bursts across the electromagnetic spectrum, and detailed theoretical modelling of localized TNRs, are necessary to determine what truly triggers these events.

#### **Online content**

Any methods, additional references, Nature Research reporting summaries, source data, extended data, supplementary information, acknowledgements, peer review information; details of author contributions and competing interests; and statements of data and code availability are available at https://doi.org/10.1038/s41586-022-04495-6.

- 1. Bode, M. F. & Evans, A. (eds) Classical Novae 2nd edn (Cambridge Univ. Press, 2008).
- Starrfield, S., Iliadis, C. & Hix, W. R. in Classical Novae 2nd edn (eds Bode, M. F. & Evans, A.)
   77–101 (Cambridge Univ. Press, 2008).
- José, J. et al. 123–321 models of classical novae. Astron. Astrophys. 634, A5 (2020).
- Mitrofanov, I. G. in Close Binary Stars: Observations and Interpretation (eds Popper, D. M. & Ulrich, R. K.) 431–436 (D. Reidel Publishing Co., 1980).
- Fabbiano, G. et al. Coordinated X-ray, ultraviolet and optical, observations of AM Her, UGem and SS Cyg. Astrophys. J. 243, 911–925 (1981).
- Shara, M. M. Localized thermonuclear runaways and volcanoes on degenerate dwarf stars. Astrophys. J. 261, 649–660 (1982).
- Szkody, P. & Mateo, M. An unprecedented UV/optical flare in TV Columbae. Astrophys. J. 280, 729-733 (1984).
- Schwarz, H. E. et al. Outbursts in TV Columbae: Walraven photometry and CCD spectroscopy. Astron. Astrophys. 202, L16–L18 (1988).
- Hellier, C. & Buckley, D. A. H. TV Columbae in outburst: a mass transfer event? Mon. Not R. Astron. Soc. 265, 766–772 (1993).
- Šimon, V. A study of the long-term activity of five intermediate polars with accretion discs. Mon. Not. R. Astron. Soc. 505, 161–171 (2021).
- Hameury, J.-M. & Lasota, J.-P. Dwarf nova outbursts in intermediate polars. Astron. Astrophys. 602, A102 (2017).
- Lewin, W. H. G., van Paradijs, J. & Taam, R. E. X-ray bursts. Space Sci. Rev. 62, 223–389 (1993).
- Bildsten, L. in The Many Faces of Neutron Stars NATO Advanced Study Institute (ASI) Series C Vol. 515 (eds Buccheri, R. et al.) 419 (Kluwer Academic, 1998).
- Galloway, D. K. et al. Thermonuclear (Type I) x-ray bursts observed by the Rossi X-Ray Timing Explorer. Astrophys. J. Suppl. Series 179, 360–422 (2008).
- Augusteijn, T. et al. Periodicities in the optical brightness variations of the intermediate polar TV Columbae. Astron. Astrophys. Suppl. 107, 219-233 (1994).
- Rana, R. R. et al. Periodicities in the X-ray intensity variations of TV Columbae: an intermediate polar. Astron. J. 127, 489–500 (2004).
- Lopes de Oliveira, R. & Mukai, K. Developing the physical understanding of intermediate polars: an X-ray study of TV Col and V2731 Oph. Astrophys. J. 880, 128 (2019).
- Thorstensen, J. R. Orbital studies of cataclysmic binaries. II. Three objects from the Palomar-Green sample. Astron. J. 91, 940–950 (1986).
- Baskill, D. S., Wheatley, P. J. & Osborne, J. P. The complete set of ASCA X-ray observations of non-magnetic cataclysmic variables. Mon. Not. R. Astron. Soc. 357, 626–644 (2005).
- Reimer, T. W. et al. The intermediate polar El UMa: a prepolar cataclysmic variable. Astrophys. J. 678, 376–384 (2008).

- Kozhevnikov, V. P. Detection of a coherent oscillation with a 769.63-s period in the intermediate polar El UMa (PG 0834+488). Astron. Lett. 36, 554-568 (2010).
- Shappee, B. J. et al. The man behind the curtain: X-rays drive the UV through NIR variability in the 2013 Active Galactic Nucleus Outburst in NGC 2617. Astrophys. J. 788, 48 (2014).
- Gomez, S. et al. Dynamical modelling of CXOGBS J175553.2-281633: a 10 h long orbital period cataclysmic variable. Mon. Not. R. Astron. Soc. 502, 48–59 (2021).
- 24. Gaia Collaboration. The Gaia mission. Astron. Astrophys. 595, A1 (2016).
- Gaia Collaboration. Gaia Early Data Release 3. Summary of the contents and survey properties. Astron. Astrophys. 649, A1 (2021).
- Lasota, J.-P. The disc instability model of dwarf novae and low-mass X-ray binary transients. New Astron. Rev. 45, 449–508 (2001).
- 27. Hameury, J. M. A review of the disc instability model for dwarf novae, soft X-ray transients and related objects. *Adv. Space Res.* **66**, 1004–1024 (2020).
- Scaringi, S. et al. Magnetically gated accretion in an accreting 'non-magnetic' white dwarf. Nature 552, 210–213 (2017).
- Scaringi, S. et al. An accreting white dwarf displaying fast transitional mode switching Nat. Astron. 6, 98–102 (2022).
- Günther, M. N. et al. Stellar flares from the first TESS data release: exploring a new sample of M dwarfs. Astron. J. 159, 60 (2020).
- 31. Doyle, L., Ramsay, G. & Doyle, J. G. Superflares and variability in solar-type stars with TESS in the southern hemisphere. *Mon. Not. R. Astron. Soc.* **494**, 3596–3610 (2020).
- Feinstein, A. D. et al. Flare statistics for young stars from a convolutional neural network analysis of TESS data. Astron. J. 160, 219 (2020).
- Schmitt, J. H. M. M. et al. Superflares on AB Doradus observed with TESS. Astron. Astrophys. 628, A79 (2019).
- Ilin, E. et al. Giant white-light flares on fully convective stars occur at high latitudes. Mon. Not. R. Astron. Soc. 507, 1723–1745 (2021).
- 35. Liller, W. & Shao, C. Y. *IAU Circular 2848: N Cyg 1975* (1975); http://www.cbat.eps.harvard.edu/iauc/02800/02848.html
- AAVSO Alert Notice 752: Rare Outburst of Recurrent Nova RS Ophiuchi (2021); https://www.aavso.org/aavso-alert-notice-752
- Galloway, D. K. et al. The Multi-Instrument Burst ARchive (MINBAR). Astrophys. J. Suppl. Ser. 249, 32 (2020).
- van Paradijs, J. et al. A unique triple-peaked type-1 X-ray burst from 4U/MXB 1636-53.
   Mon. Not. R. Astron. Soc. 221, 617-623 (1986).
- Zhang, G. et al. A very rare triple-peaked type-I X-ray burst in the low-mass X-ray binary 4U 1636-53. Mon. Not. R. Astron. Soc. 398, 368–374 (2009).
- Bhattacharyya, S. & Strohmayer, T. E. An unusual precursor burst with oscillations from SAX J1808.4-3658. Astrophys. J. 656, 414–419 (2007).
- Nauenberg, M. Analytic approximations to the mass-radius relation and energy of zero-temperature stars. Astrophys. J. 175. 417–430 (1972).
- Boirin, L. et al. Discovery of X-ray burst triplets in EXO 0748-676. Astron. Astrophys. 465, 559–573 (2007).
- Linares, M. et al. Millihertz quasi-periodic oscillations and thermonuclear bursts from Terzan 5: a showcase of burning regimes. Astrophys. J. 748, 82 (2012).
- Keek, L. & Heger, A. Thermonuclear bursts with short recurrence times from neutron stars explained by opacity-driven convection. Astrophys. J. 842, 113 (2017).
- 45. Colgate, S. A. Early gamma rays from supernovae. Astrophys. J. 187, 333-336 (1974).
- Kuulkers, E. et al. A half-a-day long thermonuclear X-ray burst from KS 1731-260. Astron. Astrophys. 382, 503-512 (2002).
- Ferrario, L., de Martino, D. & Gänsicke, B. T. Magnetic white dwarfs. Space Sci. Rev. 191, 111–169 (2015).
- Frank, J., King, A. R. & Raine, D. J. Accretion Power in Astrophysics 3rd edn (Cambridge Univ. Press, 2002).
- Duffy, C. et al. The return of the spin period in DW Cnc and evidence of new high state outbursts. Mon. Not. R. Astron. Soc. 510, 1002–1009 (2021).

**Publisher's note** Springer Nature remains neutral with regard to jurisdictional claims in published maps and institutional affiliations.

© The Author(s), under exclusive licence to Springer Nature Limited 2022

## **Methods**

#### X-Shooter spectrum of ASASSN-19bh

The Very Large Telescope (VLT) observed ASASSN-19bh on 1 October 2021 with X-Shooter  $^{50}$ . Exposure times were set at 790 s for both the UBV and visible arm of the spectrograph, and 3  $\times$  100 s for the near-infrared arm. The data reduction was carried out with the ESO Reflex pipeline  $^{51}$  v.3.5.0. The pipeline performs the standard reduction, including flat fielding, bias and dark corrections, wavelength calibration and rectification of the spectrum and extraction. The flux calibration was performed using a standard star observed on the same night. No telluric correction was performed. Extended Data Figure 1 shows the resulting spectrum in the relevant wavelength ranges of 3,900–4,900 Å and 5,800–6,700 Å.

#### **Data sources**

The TESS data for TV Col, EI UMa and ASASSN-19bh were obtained from The Barbara A. Mikulski Archive for Space Telescopes (MAST) in reduced and calibrated format. The TESS telescope/detector is sensitive to light across a wide range of wavelengths (600-1,000 nm). For all, we also retrieved ASAS-SN<sup>22,52</sup> ground-based V- and g-band available photometry. More specifically, this data set includes g-band observations for all systems that are quasi-simultaneous with the TESS data. We used this overlap to establish an approximate transformation of the TESS count rates for TV Col, EI UMa and ASASSN-19bh into standard g-band fluxes. To achieve this, we first selected the data points between TESS and ASAS-SN that were taken within 120 s of each other. These selected data points were correlated and linearly fitted. The fits were performed independently on each half of a TESS sector in order to minimize systematic count rate offsets induced between different observation sectors and in between data downlinks. The resulting linear fits allow the TESS count rates to be converted into equivalent ASAS-SN g-band fluxes, but we note that this method does not take into account any bolometric correction. We then adopt the Gaia parallax measurements<sup>24,25</sup> for TV Col, EI UMa and ASASSN-19bh to convert the fluxes into luminosities as shown in Figs. 1 and 2. To compute the peak luminosities of each burst we have subtracted an estimate of the quiescent luminosity level. This was measured as the mean luminosity throughout the 1 day preceding each burst. The burst energies have also been estimated using the same quiescent luminosity subtraction. The long-term ASAS-SN lightcurves, and the TESS calibrated photometry, are shown in Extended Data Fig. 2.

To better compare the bursts observed by TESS with those observed at X-ray wavelengths in type-I X-ray bursts, we have retrieved archival data on 4U 1636-536 and SAX J1808.4-3658. Extended Data Figure 3 shows insets of bursts from each system compared with the TV Col and ASASSN-19bh lightcurves observed by TESS. The data for 4U 1636-536 are from an EXOSAT-ME observation  $^{38}$  performed on 9 August 1985. The data for SAX J1808.4-3658 are from an RXTE-PCA observation  $^{40}$  performed on 19 October 2002.

#### Timing analysis of TESS data

TV Col is known to display evidence of both negative and positive superhumps  $^{53}$ . The former signal suggests the presence of a tilted and precessing accretion disk, whereas the latter is related to a tidally deformed accretion disk, which can occur when the outer disk edge extends to the 3:1 resonance radius with the donor star  $^{54}$ . When this happens, the positive superhump excess ( $\varepsilon = \frac{(P_{Sh} - P_{Orb})}{P_{Orb}}$ , where  $P_{Sh}$  and  $P_{Orb}$  are the positive superhump and orbital period, respectively) can be used to infer the binary mass ratio. In the case of TV Col, the inferred mass ratio is large ( $q \approx 0.92$ ) compared to other AWDs  $^{54}$ . No positive or negative superhump periods have been reported in the literature for either EI UMa or ASASSN-19bh.

Lomb-Scargle periodograms<sup>55,56</sup> of TV Col were computed using TESS cycle 1 and cycle 3 data. The periodogram for cycle 1 data was computed using the available 120 s cadence data, whereas we used the

available 20 s cadence data for cycle 3. As the three bursts observed during cycle 3 introduce excess power at low frequencies owing to red-noise leakage, we excluded the cycle 3 data in the time range 2,195.5 < TJD < 2,202.5, where TJD is the TESS Julian date (BJD-2457000). Extended Data Figure 4 shows the computed normalized periodograms. Cycle 1 data display strong signals at the orbital frequency of  $f_{\rm orb} = 4.374(19)$  cycles per day (c d<sup>-1</sup>) (5.487 h) and several associated harmonic frequencies, consistent with reported literature values<sup>8,9,54,57</sup>.  $The \, error \, on \, the \, signal \, frequency \, has \, been \, inferred \, through \, the \, window \, denote the \, constant \, denote the error \, continuous \, denote the error \, denote$ function  $(\frac{1}{T})$ , where T is the length of the lightcurve segment). Computing the signal-to-noise ratio (S/N) of the detected signals requires prior knowledge of the shape of the underlying intrinsic broad-band noise components. In the absence of this, we use the root mean square of powers at frequencies just short and just long of the detected signal to obtain S/N > 41 for the orbital signal. A further signal at f = 40.879(19) c d<sup>-1</sup>(2,114 s) is also detected with a S/N > 5 using the same methodology as for the orbital signal. This latter signal is consistent with the beat signal between the previously published white dwarf spin signal of  $f_{\text{spin}} = 45.224 \text{ c d}^{-1} (1.911 \text{ s})^{57.58}$  and the system orbital period. The cycle 1 periodogram also displays strong signals at the system orbital frequency and related harmonics. We also detect a superorbital frequency at  $f_{so} = 0.257$  c d<sup>-1</sup> with S/N > 10 and the associated negative superhumps resulting from the superorbital-to-orbital beat frequency at  $f_{-}$  = 4.630(19) c d<sup>-1</sup> with S/N > 40.

Periodograms were computed using the TESS 120 s cadence data of EI UMa. Extended Data Figure 5 shows the periodogram obtained before the bursts commenced (TJD < 1,845.1) and after the bursts occurred (TJD > 1,856). During the preburst stage we detect signatures of a positive superhump at  $f_+ = 3.08(39)$  c d<sup>-1</sup> with S/N > 6. During the postburst phase we detect the system orbital period  $f_{\text{orb}} = 3.729(92) \text{ c d}^{-1}$ (6.435 h) with S/N > 7 and the spin-to-orbital beat frequency f=112.240(92) c d<sup>-1</sup> (769.8 s) with S/N > 4, both consistent with values reported in the literature<sup>20,21</sup>. We use the detected positive superhump observed before the burst to infer the period excess of EI UMa to be  $\epsilon = 0.208$ . To date, we believe this constitutes the largest period excess detected in an AWD, surpassing that of TV Col<sup>53</sup>. We note, however, that the positive superhump-to-mass ratio relation has not been calibrated for  $\epsilon > 0.1$ . Furthermore, large mass-ratio binaries are not necessarily expected to follow the same superhump relation as low mass-ratio binaries. It is interesting to note, however, that the positive superhump signal in EI UMa disappears after the two bursts. This may be due to the localized TNRs disrupting the disk geometry, thus dissipating and eventually quenching the positive superhump signal. A similar mechanism is also invoked in explaining some of the variability observed immediately following intermediate duration type-IX-ray bursts<sup>59,60</sup>.

Periodograms of ASASSN-19bh using 120 s cadence data did not reveal any clear coherent significant signals. However, a sinusoidal signal with periodicity of approximately 4.5 days and approximately 20% amplitude is observed throughout all the TESS observations before to the flare onset. This signal is reminiscent of what is also observed in TV Col during quiescence and is possibly related to a tilted retrogradely precessing accretion disk as observed in other AWDs<sup>61</sup>.

We note that whereas both TV Col and EI UMa are known to be magnetic AWDs from the direct detection of their spin periods and hard X-ray emission  $^{62\text{-}64}$ , the magnetic nature of the white dwarf in ASASSN-19bh is not known. If it were magnetic, the larger distance to ASASSN-19bh of approximately 1.5 kpc compared to TV Col (approximately 514 pc) and EI UMa (approximately 1.14 kpc) would make the X-ray emission fainter, plausibly explaining the current non-detection in the X-ray band. Future observations will reveal whether ASASSN-19bh is a magnetic AWD, strengthening the evidence for magnetically confined and localized TNRs.

#### Localized TNR from ballistic impact

When the white dwarf surface magnetic field is  $B > 10^6$  G, the spinning magnetosphere is able to govern the accretion dynamics and funnel

material onto a smaller surface fractional area creating an accretion column onto the white dwarf magnetic poles 48,65,66. In practice the disk truncation radius will depend on the combination of white dwarf spin. mass transfer rate through the disk and white dwarf surface magnetic field. If the spinning magnetospheric barrier resides within the disk circularization radius, then an accretion disk can form and be truncated at the inner-disk edges. If, on the other hand, the magnetospheric barrier resides at radii larger than the disk circularization radius, then material from the donor star is able to latch onto field lines before it is able to form a disk. In the most extreme cases, when the white dwarf surface magnetic field is  $B > 10^7$  G, the white dwarf spin and binary orbital period become synchronized and mass transfer proceeds directly from the donor star onto the white dwarf magnetic poles along magnetic field lines. The infalling material will exert a ram pressure on the white dwarf magnetic poles from the ballistic impact,  $P_{\rm ram} \propto \dot{M} f^{-1} M_{\rm WD}^{1/2} R_{\rm WD}^{-5/2}$ , where M is the mass accretion rate onto the surface, and  $M_{\rm WD}$  and  $R_{\rm WD}$  are the white dwarf mass and radius, respectively  $^{48}$  . The factor f is the surface fractional area of the impact on the white dwarf,  $f = A_{col}/A_{WD}$ . If the pressure at the base of the accretion column is comparable to the critical pressure, such that  $P_b \approx P_{\text{ram}} \approx P_{\text{crit}}$ , then it may be possible to initiate localized fusion simply from the large pressure of the incoming ballistic accretion flow. For this to happen, however, a very small fractional area of  $f < 10^{-10}$  is required even to reach the lowest critical pressure of  $P_{\text{ram}} \approx P_{\text{crit}} \approx 10^{18} \text{ dyn cm}^{-2}$ .

The fractional area onto which the flow impacts the white dwarf surface will depend on how far away the magnetospheric disk truncation is, which in turn depends on the white dwarf's magnetic field strength and mass accretion rate. The inhomogeneous accretion flow scenario (referred to as the 'bombardment' scenario in the low mass transfer regime)<sup>48,65</sup>, which has been successful in explaining several observations of strongly magnetic AWDs, envisages three distinct accretion fractional areas. In this model, the accretion flow onto the magnetic poles does not necessarily have to be homogeneous, but may occur (at least occasionally) through higher density parcels of material referred to as 'blobs'. The largest fractional area considered is  $f_{zone}$ , which is related to the region over which accretion takes place onto the magnetic poles. The smallest fractional area considered,  $f_{acc}$ , is related to the impact region of the individual blobs of material raining down onto  $f_{\text{zone}}$ . These blobs are expected to be more elongated when latching onto field lines from larger magnetospheric radii and, because of their smaller fractional area and higher density, are also expected to bury themselves several scale heights below the white dwarf photo sphere <sup>48</sup>. The fractional area  $f_{\rm eff}$  is related to the effective radiative area of the energy released within the white dwarf photosphere from the buried blobs, which have impacted the white dwarf on  $f_{\rm acc}$ . Thus, in general, the bombardment scenario defines three accretion fractional areas such that  $f_{\text{acc}} \ll f_{\text{eff}} < f_{\text{zone}}$ .

The smallest fractional areas  $(f_{acc})$  in magnetic AWDs can occur in so-called polars, where the accretion stream from the secondary can become highly inhomogeneous as it travels along the field lines directly from the donor star. In this most extreme case the model<sup>47,48,65</sup> can allow for the filamentary blobs to have an  $f_{\rm acc} \approx 10^{-7}$  on impact, at least three orders of magnitude larger than what is required to reach  $P_{\text{ram}} \approx P_{\text{crit}}$ . Furthermore, assuming the rapid bursts are the result of a localized TNR burning through an accreted hydrogen-rich filament, we can use the hydrogen-to-helium conversion of approximately 1016 erg g-1 released during the carbon-nitrogen-oxygen cycle<sup>2,3</sup> to infer that the bursts would burn a mass in excess of  $1 \times 10^{-11} M_{\odot}$ . This would then imply that the filaments are of comparable mass, which is excessively high for individual accretion events. Finally, because the white dwarfs in both TV Col and EI UMa are known to be asynchronously rotating with respect to their binary orbits, accretion onto the magnetic field lines is expected to be by a disk rather than from a stream directly from the donor. The magnetically confined accretion flow is thus expected to be more homogeneous than that in polars. It is thus highly unlikely

that the required fractional area of  $f_{acc} < 10^{-10}$  can be achieved to reach  $P_{ram} \approx P_{crit}$  and ignite a localized TNR.

## **Data availability**

The data collected by the TESS mission used in this study can be obtained from MAST in reduced and calibrated format (https://mast.stsci.edu/). The ASAS-SNg- and V-band magnitudes can be obtained from the ASAS-SN Sky Patrol webpage (https://asas-sn.osu.edu/). The RXTE-PCA data of SAX J1808.4-365 and the EXOSAT-ME data of 4U 1636-536 have been retrieved from the High Energy Astrophysics Science Archive Research Center.

- Vernet, J. et al. X-shooter, the new wide band intermediate resolution spectrograph at the ESO Very Large Telescope. Astron. Astrophys. 536, A105 (2011).
- 51. Modigliani, A. et al. The X-shooter pipeline. Proc. SPIE 7737, 773728 (2010).
- Kochanek, C. S. et al. The All-Sky Automated Survey for Supernovae (ASAS-SN) Light Curve Server v1.0. Publ. Astron. Soc. Pac. 129, 104502 (2017).
- Retter, A. et al. A 6.3-h superhump in the cataclysmic variable TV Columbae: the longest yet seen. Mon. Not. R. Astron. Soc. 340, 679–686 (2003).
- Patterson, J. et al. Superhumps in cataclysmic binaries. XXV. q<sub>crit</sub>, ε(q), and mass-radius. Publ. Astron. Soc. Pac. 117, 1204–1222 (2005).
- Lomb, N. R. Least-squares frequency analysis of unequally spaced data. Astrophys. Space Sci. 39, 447–462 (1976).
- Scargle, J. D. Studies in astronomical time series analysis. II. Statistical aspects of spectral analysis of unevenly spaced data. Astrophys. J. 263, 835–853 (1982).
- Schrijver, J., Brinkman, A. C. & & van der Woerd, H. New EXOSAT observations of Tv-Columbae – preliminary results. Astron. Space Sci. 130, 261–274 (1987).
- Schrijver, J. et al. 2AO526-328 the white dwarf rotation period revealed. Space Sci. Rev. 40, 121–126 (1985).
- Degenaar, N. et al. X-ray emission and absorption features during an energetic thermonuclear X-ray burst from IGR J17062-6143. Astrophys. J. Lett. 767, 37 (2013).
- Degenaar, N. et al. Accretion disks and coronae in the X-ray flashlight. Space Sci. Rev. 214, 15 (2018).
- Ikkiewicz, K. et al. Exploring the tilted accretion disc of AQ Men with TESS. Mon. Not. R. Astron. Soc. 503, 4050–4060 (2021).
- Bird, A. J. et al. The Fourth IBIS/ISGRI Soft Gamma-ray Survey Catalog. Astrophys. J. Suppl. Ser. 186, 1–9 (2010).
- Oh, K. et al. The 105-Month Swift-BAT All-sky Hard X-Ray Survey. Astrophys. J. Suppl. Ser. 235, 4 (2020).
- Shaw, A. W. et al. Measuring the masses of magnetic white dwarfs: a NuSTAR legacy survey. Mon. Not. R. Astron. Soc. 498, 3457–3469 (2020).
- King, A. R. Accretion on to magnetic white dwarfs. Astron. Soc. Pac. Conf. Ser. 85, 23–27 (1995).
- Wickramasinghe, D. T. & Ferrario, L. Magnetism in isolated and binary white dwarfs. Publ. Astron. Soc. Pac. 112, 873–924 (2000).

Acknowledgements P.J.G. is supported by the South African National Research Foundation (NRF) SARChI grant no. 111692, D.A.H.B. acknowledges research support from the South African National Research Foundation, D.d.M. acknowledges financial support from the Italian Space Agency (ASI) and National Institute for Astrophysics (INAF) under agreements ASI-INAF I/037/12/0 and ASI-INAF n.2017-14-H.O. and from INAF 'Sostegno alla ricerca scientifica main streams dell'INAF', Presidential Decree 43/2018, from INAF 'SKA/CTA projects', Presidential Decree 70/2016, and from PHAROS COST Action N.16214, C.D. and K.I. acknowledge funding from the Science and Technology Facilities Council (STFC) consolidator grant no. ST/T000244/1, J.-P.L. was supported in part by a grant from the French Space Agency CNES. P.S. acknowledges support from National Science Foundation (NSF) grant no. AST-1514737. F.X.T. is supported by the NSF under grant no. ACI-1663684 for the MESA Project, and by the NSF under grant no. PHY-1430152 for the Physics Frontier Center Joint Institute for Nuclear Astrophysics Center for the Evolution of the Elements (JINA-CEE). This paper includes data collected by the TESS mission. Funding for the TESS mission is provided by the NASA's Science Mission Directorate. Some of the data presented in this paper were obtained from the Mikulski Archive for Space Telescopes (MAST). The Space Telescope Science Institute (STScI) is operated by the Association of Universities for Research in Astronomy, Inc., under NASA contract no. NAS5-26555. Support for MAST fo non-Hubble Space Telescope data is provided by the NASA Office of Space Science by grant no. NNX09AF08G and by other grants and contracts. This paper uses data from the ASAS-SN project run by the Ohio State University. We thank the ASAS-SN team for making their data publicly available. This work has also made use of data from the European Space Agency mission Gaia (https://www.cosmos.esa.int/gaia), processed by the Gaia Data Processing and Analysis Consortium (DPAC, https://www.cosmos.esa.int/web/gaia/dpac/ consortium). Funding for the DPAC has been provided by national institutions, in particular the institutions participating in the Gaia Multilateral Agreement. The study is based on observations collected at the European Southern Observatory (ESO) under ESO-DDT programme 107,2309,001, for which we acknowledge support from the ESO Director-General.

**Author contributions** S.S. was principal investigator of the TESS proposal to obtain the data, discovered the bursts and performed the ASAS-SN luminosity calibration, co-developed the application of the bombardment model to potentially drive TNRs and led the interpretation of the bursts. P.J.G. was principal investigator of the X-Shooter proposal

to obtain the spectrum of ASASSN-19bh. Y.C. contributed details on the analogy with type-I X-ray bursts, including leading the discussions on their temporal evolution. C.F.M. reduced the X-Shooter spectrum of ASASSN-19bh. S.S., P.J.G., C.K., A.J.B., E.B., D.A.H.B., Y.C., N.D.D., D.d.M., C.D., M.F., K.I., E.K., J.-P.L., C.L., C.F.M., M.O'B., P.S. and F.X.T shared ideas, interpreted the results, commented and edited the manuscript.

Competing interests The authors declare no competing interests.

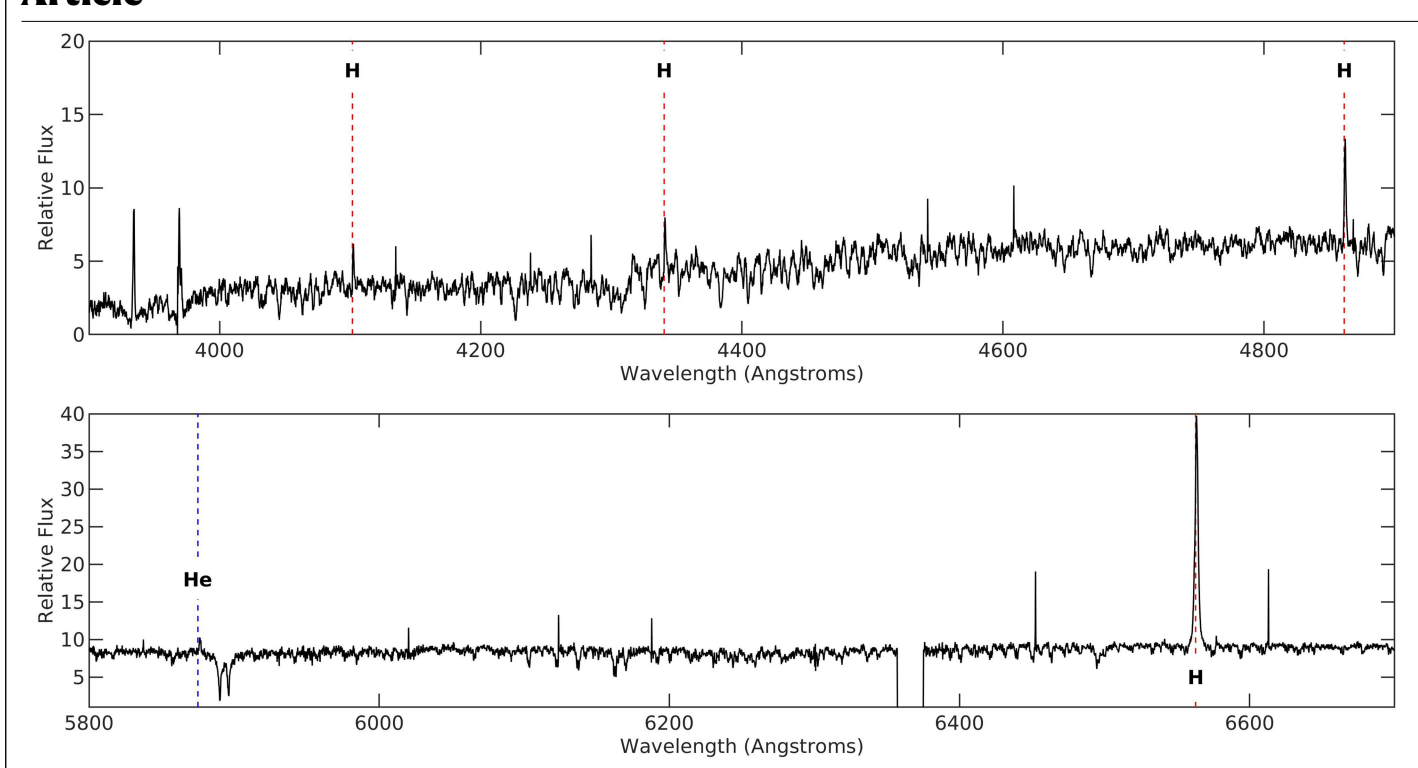
#### Additional information

 $\textbf{Supplementary information} \ The \ online \ version \ contains \ supplementary \ material \ available \ at \ https://doi.org/10.1038/s41586-022-04495-6.$ 

Correspondence and requests for materials should be addressed to S. Scaringi.

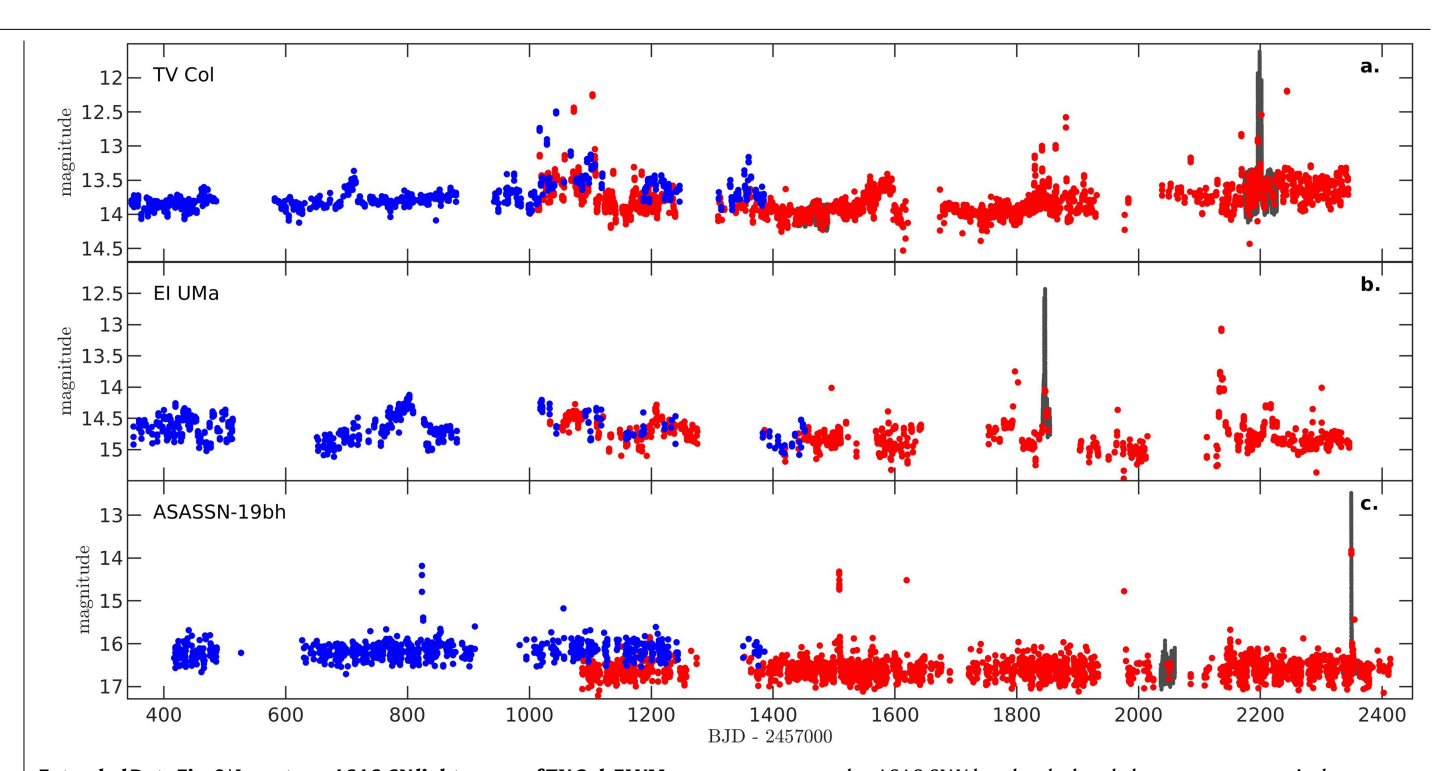
Peer review information Nature thanks Michael Shara and Erik Kuulkers for their contribution to the peer review of this work. Peer reviewer reports are available.

 $\textbf{Reprints and permissions information} \ is \ available \ at \ http://www.nature.com/reprints.$ 



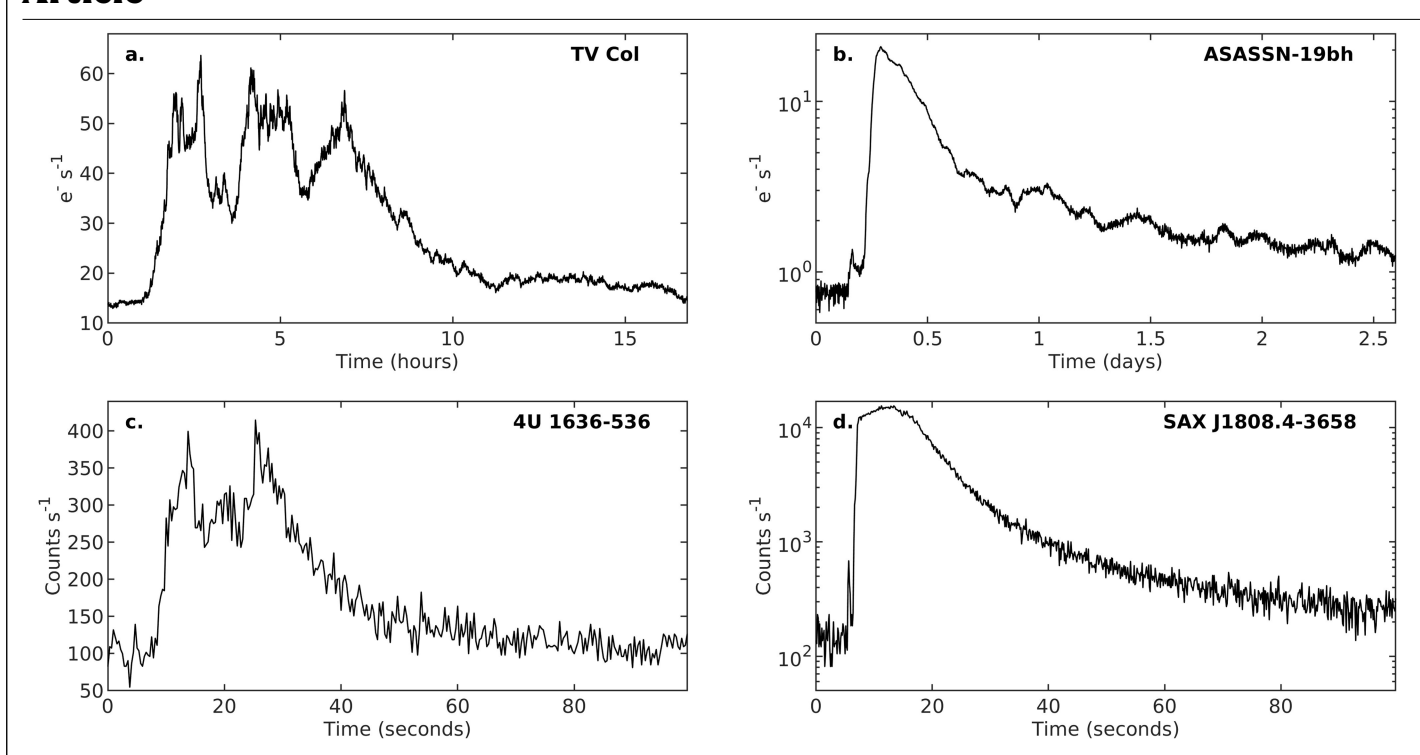
**Extended Data Fig. 1** | **X-Shooter spectrum of ASASSN-19bh. a**. X-Shooter spectrum (UBV arm) in the range 3900 Å-4900 Å. **b.** X-Shooter spectrum (VIS arm) in the range 5800 Å-6700 Å. Hydrogen Balmer-series lines are marked with the red dashed lines. The Hel 5875 Å is marked with a blue dashed line.

Call H&K emission lines can be seen blueward of 4000 Å. Numerous narrow absorption lines from the secondary are also identifiable. Narrow emission spikes in e.g. the region 6000-6200 Å are residuals from the sky subtraction.



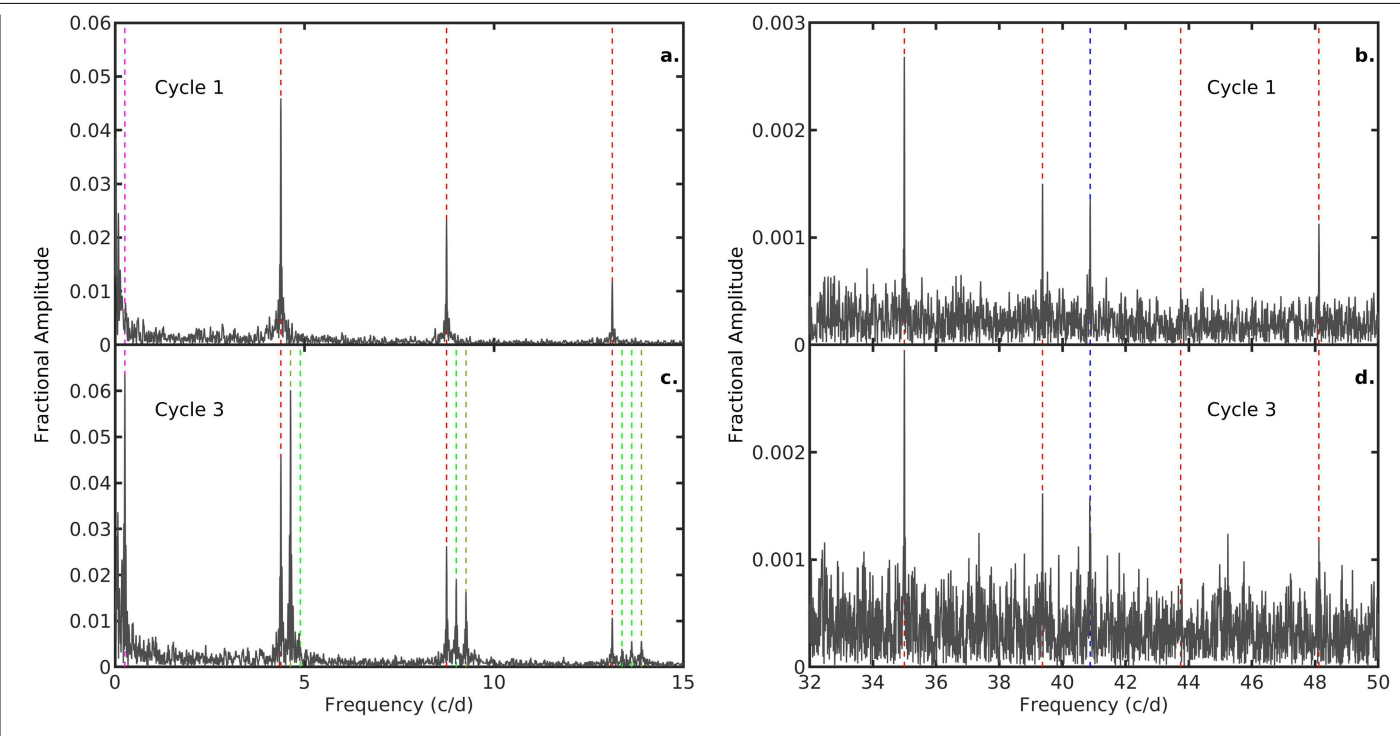
 $\label{eq:continuous} \textbf{Extended Data Fig. 2} \ | \ Long term ASAS-SN lightcurves of TV Col, El UMa, \\ \textbf{and ASASSN-19bh. a.} \ ASAS-SN lightcurve of TV Col b. \ ASASSN lightcurve of El UMa c. \ ASASSN lightcurve of ASASSN-19bh. \ In all panels the blue and red points \\ \ | \ Long term ASASSN lightcurve of ASASSN-19bh. \ | \ Long term ASASSN lightcurve of El UMa c. \ | \ Long term ASASSN lightcurve of El UMa c. \ | \ Long term ASASSN lightcurve of El UMa c. \ | \ Long term ASASSN lightcurve of El UMa c. \ | \ Long term ASASSN lightcurve of El UMa c. \ | \ Long term ASASSN lightcurve of El UMa c. \ | \ Long term ASASSN lightcurve of El UMa c. \ | \ Long term ASASSN lightcurve of El UMa c. \ | \ Long term ASASSN lightcurve of El UMa c. \ | \ Long term ASASSN lightcurve of El UMa c. \ | \ Long term ASASSN lightcurve of El UMa c. \ | \ Long term ASASSN lightcurve of El UMa c. \ | \ Long term ASASSN lightcurve of El UMa c. \ | \ Long term ASASSN lightcurve of El UMa c. \ | \ Long term ASASSN lightcurve of El UMa c. \ | \ Long term ASASSN lightcurve of El UMa c. \ | \ Long term ASASSN lightcurve of El UMa c. \ | \ Long term ASASSN lightcurve of El UMa c. \ | \ Long term ASASSN lightcurve of El UMa c. \ | \ Long term ASASSN lightcurve of El UMa c. \ | \ Long term ASASSN lightcurve of El UMa c. \ | \ Long term ASASSN lightcurve of El UMa c. \ | \ Long term ASASSN lightcurve of El UMa c. \ | \ Long term ASASSN lightcurve of El UMa c. \ | \ Long term ASASSN lightcurve of El UMa c. \ | \ Long term ASASSN lightcurve of El UMa c. \ | \ Long term ASASSN lightcurve of El UMa c. \ | \ Long term ASASSN lightcurve of El UMa c. \ | \ Long term ASASSN lightcurve of El UMa c. \ | \ Long term ASASSN lightcurve of El UMa c. \ | \ Long term ASASSN lightcurve of El UMa c. \ | \ Long term ASASSN lightcurve of El UMa c. \ | \ Long term ASASSN lightcurve of El UMa c. \ | \ Long term ASASSN lightcurve of El UMa c. \ | \ Long term ASASSN lightcurve of El UMa c. \ | \ Long term ASASSN lightcurve of El UMa c. \ | \ Long term ASASSN lightcur$ 

correspond to ASAS-SN V-band and g-band photometry respectively. Calibrated TESS data points are shown in grey. Typical uncertainties on magnitude are  $0.02.\,$ 

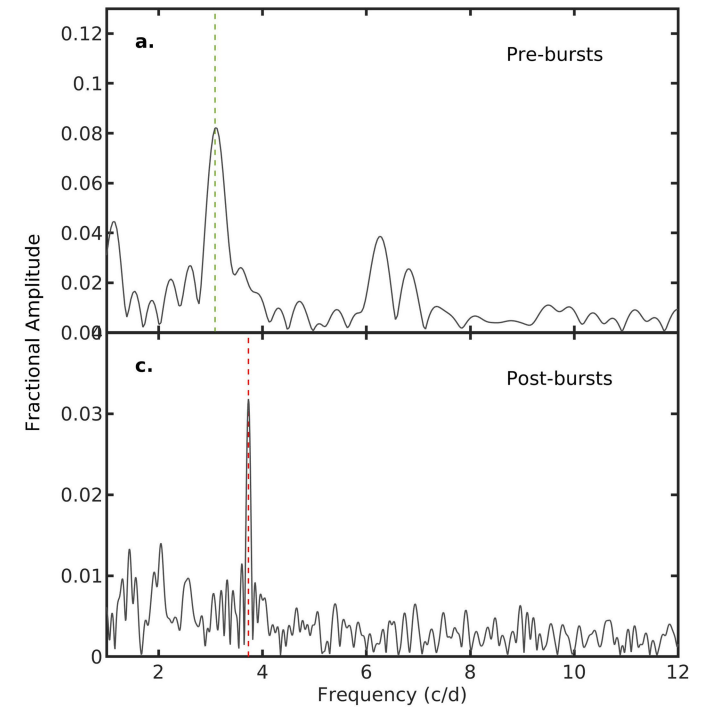


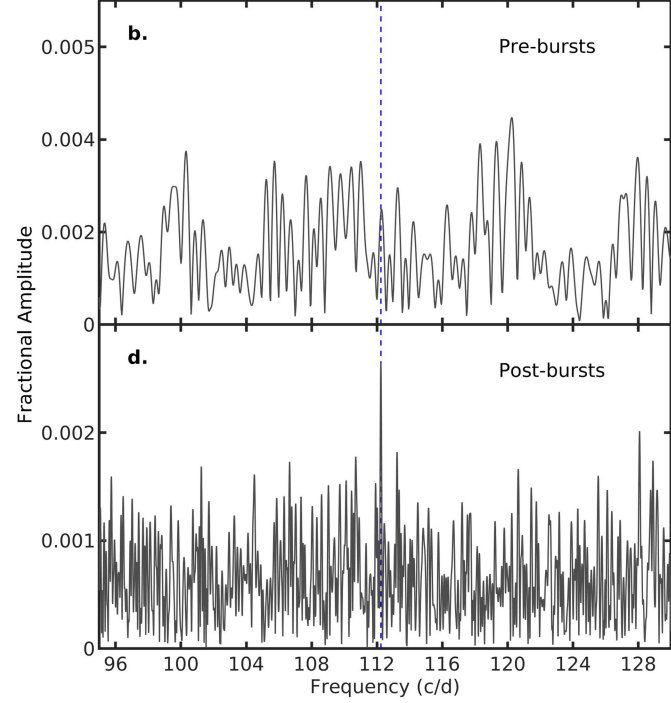
Extended Data Fig. 3 | Comparison between Type-I X-ray bursts and micronovae. a. TESS lightcurve of one of the rapid bursts observed in TV Col. b. TESS lightcurve of the rapid burst observed in ASASSN-19bh. c. EXOSAT-ME X-ray lightcurve of 4U 1636-536 of one of the Type-I X-ray bursts. Note the

similar multi-peak structure in both TV Col and 4U 1636-536. **d.** RXTE-PCA X-ray lightcurve of one rapid burst in SAX J1808.4-3658. Note the precursor present in both ASASSN-19bh and SAX J1808.4-3658. In all panels the time axis has been arbitrarily shifted.



the dashed-blue vertical lines mark the spin-to-orbital beat frequency. The dashed-magenta line marks the superorbital signal. The dashed-green lines mark the detected negative superhump, associated harmonics, and beats with the orbital frequency.





 $\label{lem:extended} \textbf{Data} \ \textbf{Fig.} \ \textbf{5} \ | \ \textbf{Lomb-Scargle periodograms} \ \textbf{of} \ \textbf{EIUMa}. \ \textbf{Periodograms} \ \textbf{using} \ \textbf{TESS} \ \textbf{data} \ \textbf{for} \ \textbf{EIUMa} \ \textbf{during} \ \textbf{Cycle} \ \textbf{2} \ (120\text{-s} \ \textbf{cadence}). \ \textbf{a}. \ \textbf{Low} \ \textbf{frequency} \ \textbf{periodogram} \ \textbf{computed} \ \textbf{before} \ \textbf{the} \ \textbf{bursts}. \ \textbf{b}. \ \textbf{High-frequency} \ \textbf{periodogram} \ \textbf{computed} \ \textbf{after} \ \textbf{computed} \ \textbf{before} \ \textbf{the} \ \textbf{bursts}. \ \textbf{c}. \ \textbf{Low-frequency} \ \textbf{periodogram} \ \textbf{computed} \ \textbf{after} \ \textbf{c}. \ \textbf{computed} \ \textbf{after} \ \textbf{c}. \ \textbf{$ 

the bursts.  ${f d}$ . High-frequency periodogram computed after the bursts. In all panels the dashed-red vertical line marks the detected orbital frequency. The dashed-blue vertical lines mark the spin-to-orbital beat frequency. The dashed-green line marks the positive superhump frequency.